Capture and inception of bubbles near line vortices

G. F. Oweis
University of Michigan, Ann Arbor, Michigan 48109-2121

I. E. van der Hout
Delft University of Technology, The Netherlands

C. Iyer
The Ford Motor Company, Dearborn, Michigan 48126-2798

G. Tryggvason
Worcester Polytechnic Institute, Worcester, Massachusetts 01609-2280

S. L. Ceccio[a)]
University of Michigan, Ann Arbor, Michigan 48109-2121

(Received 15 July 2003; accepted 26 October 2004; published online 13 January 2005)

Motivated by the need to predict vortex cavitation inception, a study has been conducted to investigate bubble capture by a concentrated line vortex of core size r_c and circulation Γ_0 under noncavitating and cavitating conditions. Direct numerical simulations that solve simultaneously for the two phase flow field, as well as a simpler one-way coupled point-particle-tracking model (PTM) were used to investigate the capture process. The capture times were compared to experimental observations. It was found that the point-particle-tracking model can successfully predict the capture of noncavitating small nuclei by a line vortex released far from the vortex axis. The nucleus grows very slowly during capture until the late stages of the process, where bubble/vortex interaction and bubble deformation become important. Consequently, PTM can be used to study the capture of cavitating nuclei by dividing the process into the noncavitating capture of the nucleus, and then the growth of the nucleus in the low-pressure core region. Bubble growth and deformation act to speed up the capture process. © *2005 American Institute of Physics*. [DOI: 10.1063/1.1834916]

I. BACKGROUND

Hydrodynamic lifting surfaces associated with propulsion and control systems often develop concentrated trailing vortices. Small bubbles (or nuclei) present in the free stream near the concentrated vortex will be drawn toward the axis of flow rotation, and if the vortex core pressure falls below the liquid vapor pressure, these small bubbles can act as nucleation sites for cavitation inception. Vortex cavitation can also occur in unsteady vortices such as those found in shear layers and jets. Arndt[1] has recently reviewed the subject of vortex cavitation.

Early vortex cavitation inception events often happen discretely in time, and this is because two conditions must be met concurrently: (i) a cavitation nucleus (a bubble) must be present in the low-pressure region of the vortex (the core) and (ii) the vortex core pressure should be low enough for this nucleus to grow explosively, or cavitate. If a nucleus already exists in the vortex core, then cavitation inception is controlled by the pressure field generated by the vortex. Transient pressure drops in the vortex core due to unsteady flow phenomena (e.g., vortex stretching) can produce the low pressures required for the explosive growth of the nucleus. If the nucleus exists outside the core region, it can move toward the vortex axis and be "captured" by the low-pressure region of the vortex. The time it takes the nucleus to move near the vortex axis is the capture time. If the time scale associated with the transient pressure drop in the vortex core is known (i.e., how long an unsteady vortex will sustain a certain level of pressure reduction), then one needs to know the capture time to identify which nuclei surrounding an unsteady vortex will lead to discrete vortex cavitation events first. The likelihood of cavitation inception in the vortex core is related (1) to the probability of the nuclei's presence within or near the vortex core and (2) to the probability that the nuclei will migrate towards the vortex axis (be captured by the vortex) in time while the transient vortex core pressure is still low enough for explosive bubble growth. The first condition is related to the concentration and size distribution of the free-stream nuclei (i.e., the nuclei number distribution), while the second condition is governed by the capture time.

The vortex-induced capture, interaction, and growth of small bubbles have been studied by several researchers experimentally and numerically using spherical bubble assumptions and also high fidelity simulation of the two phase flow field with resolved bubble shape computations. Sridhar and Katz[2] studied an entrained bubble in a vortex ring using particle image velocimetry and showed that in certain cases the entrained bubble can substantially change the structure of the vortex. Hsiao and Pauley[3] examined the capture of a cavitation nucleus by a tip vortex employing a Reynolds averaged Navier Stokes (RANS) model of the noncavitating flow along with a point-particle tracking model (PTM) to

a)Author to whom correspondence should be addressed.

describe the spherical dynamics of the nucleus. More detailed computations have been attempted by other researchers. For instance, Chahine and co-workers have used both RANS and boundary integral methods to study vortex bubble interaction.[4–7] They have shown how captured bubbles can significantly deform as they are captured by the vortex, grow and collapse.

In models of bubbles in liquid flows that employ one-way coupling between the carrier flow and the bubble, it is assumed that the presence of the bubble does not significantly alter the carrier flow field. An equation of motion for the trajectory of the bubble is solved using a force balance on the bubble. For cavitating flows, the Rayleigh-Plesset equation is employed to describe the dynamics of the cavitating bubble. Such PTM techniques often assume that the bubbles remain spherical during the bubble capture, growth, and collapse. However, as the volume of a bubble increases, the pressure and flow gradients near the vortex can cause the bubble to deform and can lead to significant modification of the forces on the bubble. Higher fidelity simulations of the bubble-flow interactions are possible, but can be computationally intensive. It would be preferable if the one-way coupled PTM can be used to yield an accurate estimate of the bubble capture times.

In the present work, we will examine the capture of a bubble by a steady line vortex for both noncavitating and cavitating conditions. We will use one-way coupled PTM computations, and also higher fidelity, fully resolved direct numerical simulation (DNS) of the two phase flow field. The DNS does not employ the one-way coupling assumption, and thus details of the bubble shape distortions and modifications to the liquid flow field can be revealed. Experimental observations of bubble capture are then compared with the predicted results of the PTM. These data are used to explore the accuracy and limitations of the one-way coupled PTM. In comparisons involving the PTM and DNS models, the same DNS flow, fluid properties, and bubble/fluid density ratio are used in the PTM. Similarly, in comparisons involving the PTM and experimental results, the experimental flow and fluid properties are used in the PTM.

II. ONE-WAY COUPLED POINT-PARTICLE TRACKING MODEL OF BUBBLE CAPTURE

The dynamics of small bubbles in a flow can be calculated assuming that their presence does not significantly alter the flow. The effect of the flow on a bubble can be determined through the equation of motion for a point particle:[8–10]

$$\rho_B V_B \frac{d\mathbf{u}_B}{dt} = V_B(\rho_B - \rho_f)\mathbf{g} - V_B \boldsymbol{\nabla} p + \frac{1}{2}\rho_f V_B\left(\frac{D\mathbf{u}}{Dt} - \frac{d\mathbf{u}_B}{dt}\right) + \mathbf{F}_D + \mathbf{F}_L + \mathbf{F}_B + \mathbf{F}_V, \tag{1}$$

where ρ_B is the bubble density, ρ_F is the fluid density, V_B is the volume of the bubble, $\mathbf{u}_B$ is the bubble velocity, $\mathbf{u}$ is the fluid velocity in the absence of the bubble at the center of the bubble (unperturbed velocity). $\mathbf{F}_D$ is the drag force, $\mathbf{F}_L$ is the lift force, $\mathbf{F}_B$ is the Basset history force, and $\mathbf{F}_V$ is the force due to volume changes. In the present analysis, the drag force is given by

$$\mathbf{F}_D = C_D \tfrac{1}{2}\rho_f A_B |\mathbf{u} - \mathbf{u}_B|(\mathbf{u} - \mathbf{u}_B), \tag{2}$$

where

$$C_D = \frac{24}{\mathrm{Re}_B}(1 + 0.197\,\mathrm{Re}_B^{0.63} + 2.6(10^{-4})\mathrm{Re}_B^{1.38}) \tag{3}$$

and $\mathrm{Re}_B = 2R|\mathbf{u} - \mathbf{u}_B|/\nu_f$ is the bubble Reynolds number based on the bubble radius R and its slip velocity.[11] We will neglect the Basset force term, as the bubble relative acceleration is expected to be small (a detailed discussion of the relative size of the Basset term is found in Maxey and Riley[8]). The force due to the bubble volume variation is given by Johnson and Hsieh[12] as

$$\mathbf{F}_V = 2\pi R^2 \rho(\mathbf{u} - \mathbf{u}_B)\frac{dR}{dt}. \tag{4}$$

The buoyancy, pressure gradient, and added mass terms also appear in Eq. (1), with an added mass coefficient of $1/2$ for spherical bubbles. We will ignore the buoyancy force, the Basset force, and the bubble volume variation term in the PTM computations. The lift force on the bubble is related to the slip velocity and the circulation of the unperturbed fluid at the center of the bubble

$$\mathbf{F}_L = C_L \frac{1}{2}\rho_f A_B |\mathbf{u} - \mathbf{u}_B|(\mathbf{u} - \mathbf{u}_B) = \frac{3}{8}\rho_f V_B C_L \frac{(\mathbf{u} - \mathbf{u}_B) \times \omega}{\alpha}, \tag{5}$$

where $\alpha = |\omega|R/|\mathbf{u} - \mathbf{u}_B|$ is the dimensionless shear rate and ω is the fluid vorticity of the undisturbed flow at the center of the bubble. The lift coefficient is a function of both the shear and vorticity. Auton[13] and Auton, Hunt, and Prud'homme[14] showed that for weak shear ($\alpha \ll 1$) the lift coefficient is given by

$$C_{L,A} = \tfrac{4}{3}\alpha. \tag{6}$$

Saffman[15] showed that, for low Reynolds numbers ($\mathrm{Re}_B < 20$),

$$C_{L,S} = 5.82\,\mathrm{Re}_B^{-0.5}\alpha^{0.5}. \tag{7}$$

For higher Reynolds numbers, Dandy and Dwyer[16] used numerical analysis to show that for $0.0005 < \alpha < 0.4$ and $\mathrm{Re}_B > 20$,

$$C_{L,D} \approx 0.3\alpha. \tag{8}$$

Finally, Sridhar and Katz[17] experimentally determined the lift coefficient on bubbles with diameters between 500 and 800 μm and $20 < \mathrm{Re}_B < 80$, and found relatively high lift coefficients

$$C_{L,\mathrm{SK}} = 0.59\alpha^{0.25}. \tag{9}$$

In the present work, we will compare results produced using these different formulations.

To determine the volume variation for a cavitating spherical bubble, the Rayleigh-Plesset equation given is used to determine the time-varying bubble radius, $R(t)$:

$$R\frac{d^2R}{dt^2}+\frac{3}{2}\left(\frac{dR}{dt}\right)^2=\frac{1}{\rho_f}\left(p_V+p_{\mathrm{GI}}\left(\frac{R_O}{R}\right)^{3k}-p_B-\frac{2\overline{\sigma}}{R}-\frac{4\mu_f}{R}\frac{dR}{dt}\right). \quad (10)$$

This relation is derived for a spherical bubble in an unbounded fluid, and p_B is the pressure far away from the bubble, p_{GI} is the pressure of the noncondensable gas initially in the bubble when its radius is R_0, k is the polytropic exponent for the noncondensable gas within the bubble, and $\overline{\sigma}$ is the surface tension. For the point-particle-tracking model, p_B is taken as the local fluid static pressure at the location of the bubble center. If the bubble is small and the pressure gradients near the bubble are mild, then $\nabla p\cdot R/p \ll 1$ at the bubble center, and we may model $p_B \approx p$.

III. GAUSSIAN VORTEX MODEL

We will consider the capture of bubbles by a Gaussian vortex of total circulation Γ_O and core radius r_C. Also known as Lamb-Oseen vortex, the tangential velocity as a function of the radial distance from the axis r is given by

$$u_\theta(r)=\frac{\Gamma_O}{2\pi r}(1-e^{-\eta_1(r/r_C)^2}) \quad (11)$$

and the maximum tangential velocity u_C occurs at r_C and is given by

$$u_C=\eta_2\frac{\Gamma_O}{2\pi r_C}, \quad (12)$$

where $\eta_1=1.255$ and $\eta_2=0.715$. The pressure depression at the vortex centerline $r=0$ is given by

$$p(r)-p_\infty=\int_\infty^\theta -\frac{\rho_f u_\theta^2(r)}{r}dr=-\rho_f\left(\frac{\Gamma_O}{2\pi r_C}\right)^2 f\left(\frac{r}{r_C}\right), \quad (13)$$

where

$$f\left(\frac{r}{r_C}\right)=\left(\frac{-1}{2(r/r_C)^2}\right)\begin{bmatrix}-1+2e^{-\alpha(r/r_C)^2}-e^{-2\alpha(r/r_C)^2}\\ -2\alpha(r/r_C)^2Ei[\alpha(r/r_C)^2]\\ +2\alpha(r/r_C)^2Ei[2\alpha(r/r_C)^2]\end{bmatrix}. \quad (14)$$

At the vortex core,

$$p_C-p_\infty=-\rho_f\left(\frac{\Gamma_O}{2\pi r_C}\right)^2 f(0)=-\eta_3\rho_f\left(\frac{\Gamma_O}{2\pi r_C}\right)^2, \quad (15)$$

where $\eta_3=f(0)=0.870$.[18] Here, we are neglecting the possibility that there may be nonuniform flow along the vortex axis.

The vortex Reynolds number is

$$\mathrm{Re}_C=\frac{u_C r_C}{\upsilon_f}. \quad (16)$$

The Weber number of a bubble with radius R_O is

$$\mathrm{We}=\frac{\rho_f R_O u_C^2}{2\overline{\sigma}}. \quad (17)$$

The vortex cavitation number is defined as

$$\sigma_\infty=\frac{p_\infty-p_V}{\frac{1}{2}\rho_f u_C^2}. \quad (18)$$

IV. DIRECT NUMERICAL SIMULATIONS OF BUBBLE DYNAMICS

It is possible to classify the numerical methods used to solve for cavitating flows into three categories: mixed-fluid methods, discontinuous interface methods, and finite thickness interface methods. The mixed-fluid approach treats water and vapor as two different fluids and employs an additional equation for void fraction. This method does not resolve the individual bubbles, and an example is found in Kubota, Kato, and Yamaguchi.[19] Discontinuous interface models describe the system as two different flows separated by the interface, and the method can be modified to examine individual bubbles (see Deshpande, Feng, and Merkle[20]). The front tracking method used in this study falls under the third category. Front tracking works for multifluid, incompressible flows, and in this method the thin density interface between fluids is tracked explicitly by advancing the density field with a separate transport equation superimposed upon the Navier-Stokes equation. The DNS front-tracking method used in this study was developed by Unverdi and Tryggvason[21] and improved by Esmaeeli and Tryggvason.[22,23] A single Navier-Stokes equation with variable density and viscosity is solved for the entire domain, and the surface tension is added as a body force concentrated at the fluid interfaces. The fluids inside and outside the bubbles are taken to be Newtonian, and the flow is incompressible and isothermal, so that the densities and viscosities are constant within each phase. The unsteady, viscous, incompressible Navier-Stokes equations are solved on a fixed staggered grid, while the interface between the bubble and liquid is explicitly represented by a separate, unstructured grid that moves through the stationary one. The front (interface) keeps the density and viscosity discontinuities sharp and also provides a way to calculate the surface tension. The numerical scheme used is a conservative second-order accurate, centered difference scheme for spatial variables, and explicit second-order time integration. For the cavitating bubbles the interior pressure is specified and replaces the incompressibility condition there. Yu, Ceccio, and Tryggvason[24] used this front tracking method to examine the collapse of bubbles in shear flow, and developed the model used here. Resolution and accuracy studies for the cavitation models were reported in that study. For an extensive review of the basic method, see Tryggvason *et al.*[25]

V. EXPERIMENTAL SETUP

Single cavitation bubbles were created by focusing a pulsed infrared laser beam near a steady line vortex emanating from the tip of a hydrofoil. The facility used in this study is the University of Michigan 9-Inch Cavitation Tunnel. The water tunnel has a circular contraction downstream of a series of flow management screens with contraction area ratio of 6.4:1. The test section has a 22.9 cm diameter round inlet

that is then faired into a rectangular test section with widely rounded corners. Four acrylic windows (93.9 by 10.0 cm^2 viewing area) permit optical access to the test section flow. The flow in the test section can be operated at pressures from vapor pressure to ≈200 kPa. The average velocity in the test section is variable up to 18 m/s. A deaeration system was used to vary the dissolved gas content of the flow, and the inlet tunnel water is filtered to 1 μm. Details of the experimental setup and the laser bubble generation in the vortex can be found in Oweis *et al.*[18]

A vortical flow was created using a cambered hydrofoil mounted to a side window of the test section. The hydrofoil had a rectangular platform of 9.5 cm span and 16.8 cm chord. The tip of the hydrofoil was truncated with sharp edges. The hydrofoil mount allowed continuous changes of the incident flow angle. A series of tip and trailing edge vortices were shed near the tip, and these vortices merged to form a single vortex within one-half chord length downstream of the trailing edge. Measurements of the bubble/vortex interactions were taken at a free-stream velocity of 10 m/s and a variety of pressures. The dissolved oxygen content was measured with an Orion Model 810 oxygen meter. In order to reduce the number of free-stream nuclei, the free-stream gas content was reduced to below 1.5 ppm during the measurements. Natural hydrodynamic cavitation occurred at various locations along the vortex axis downstream of the location of vortex roll up. However, at such low air content, the event rate of this type of cavitation was relatively low (<0.1 event per second), and did not affect the conduct of the experiment.

Planar particle imaging velocimetry (PIV) was used to measure the vortical flow field at a station 9.0 cm downstream of the trailing edge. A double-pulsed light sheet 9 mm thick was created perpendicular to the mean flow direction using two pulsed Nd:YAG (YAG—yttrium aluminum garnet) lasers (Spectra Physics model Pro-250 Series). 15.3 μm average diameter silver coated glass spheres were used to seed the flow. An acrylic prism was optically mounted to a window of the test section for viewing the light sheet with reduced optical distortion. Double-pulsed images of the light sheet were acquired with a LaVision Inc. cross correlation digital camera with 1280×1024 pixels. Optical distortion of the planar light sheet image was corrected through a calibration procedure that employed the imaging of a regular grid in the location of the light sheet plane. Velocity vectors were produced from the double-pulsed images using the image analysis software DAVIS6.0.4. Multipass vector extraction scheme with a final window size of 32×32 pixels and 12% window overlap was used to produce 41×27 in plane velocity vectors at 0.62 mm spacing. Since the camera-imaging plane was not parallel to the light sheet and it had an angular shift of 45° with the horizontal direction, this velocity component was corrected by knowledge of the camera angle and the tunnel free-stream velocity. Image sequences of bubbles inside the vortex core indicated the axial velocity in the vortex core was nearly uniform and close to the free-stream speed.

A Gaussian vortex velocity profile was fitted to the PIV measurements, and the fitted vortex core radius was r_C = 5.6 mm and its strength was Γ_O = 0.290 m^2/s (see Oweis *et al.*[18] for additional details). Examination of the instantaneous images indicated that the vortex core did not wander significantly. The amplitude of wandering was consistently less than 10% of r_C. Consequently, no correction for vortex wandering was needed, as discussed by Boulon *et al.*[26] and Oweis and Ceccio.[27]

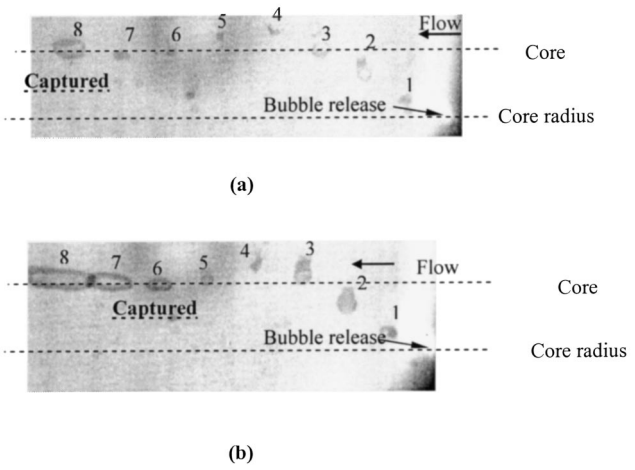

FIG. 1. (a) Eight images of a laser-induced bubble as it is captured by the vortex for cavitation number, σ_∞ = 3.0. The release position of the bubble, r_x/r_c = 1. The delay between each image is 350 μs. The capture time, t^* = 1.25. The bubble size, r_c/R_0 = 6. (b) Same as (a) but with the capture time t^* = 0.9 and bubble size r_c/R_0 = 10.

Optically stimulated cavitation bubbles were created near the vortex core. The infrared beam from a pulsed Nd-YAG laser (Quanta Ray PRO-250) was expanded through a set of spherical lenses to a diameter of ≈75 mm, and then focused into a very thin focal volume in the water tunnel test section. The 10 ns laser pulse had a wavelength of 1064 nm and maximum energy of 280 mJ. An inertial vapor bubble grows explosively at the laser focal point to a maximum volume, and then collapses violently. The bubble may rebound after its initial collapse, and bubble fragmentation and coalescence may also result after collapse. The time span of the inertial vapor bubble from the instance the laser is introduced until its violent collapse is very short and is on the order of 100–200 μs. The resulting stabilized bubble after the initial stages of violent growth and collapse is then used for the bubble/vortex capture studies. By adjusting the lens system, the bubble could be introduced at varying locations relative to the vortex axis. By varying the free-stream pressure and laser energy, the size of the laser-induced bubble could be coarsely controlled. Images of the bubble were observed with a Cooke Corp. "FlashCam" digital camera. The camera had an effective resolution of 750×240 pixels and could record up to ten consecutive exposures on the same frame, with controllable exposure times and interexposure delays. A pulse delay generator (SRS model DG535) was used to trigger the camera at varying time delays from the laser light pulse.

Figures 1(a) and 1(b) show multiple exposures of two laser induced bubbles as they are captured by the steady line vortex. The bubbles are introduced at the outer edge of the

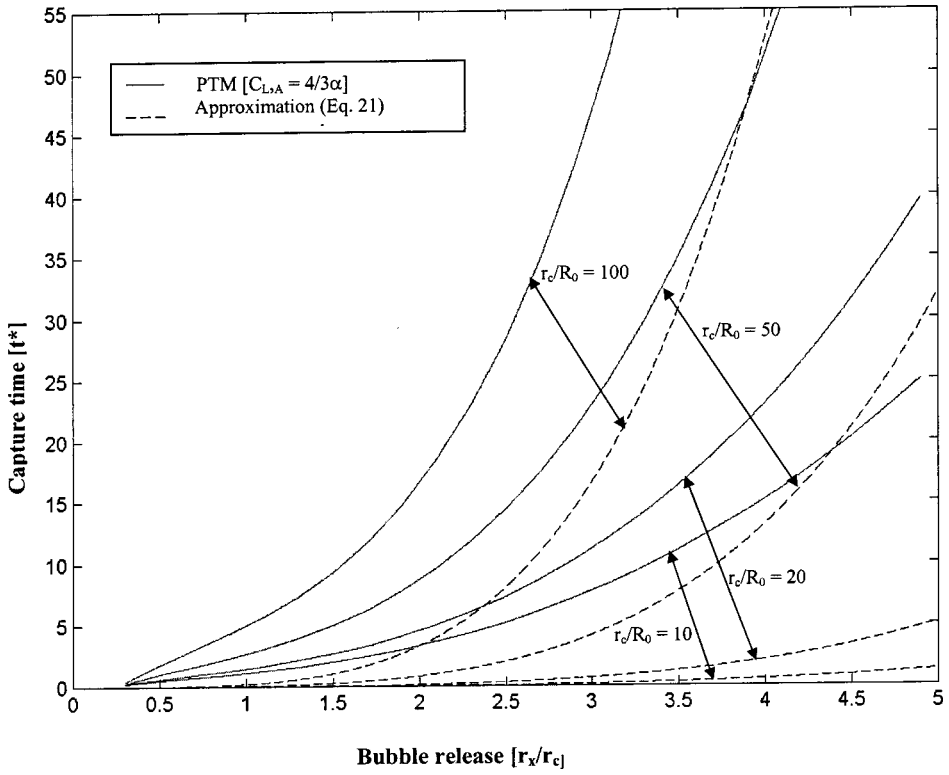

FIG. 2. Bubble capture time t^* vs the release position r_X/r_C for varying bubble sizes r_C/R_O computed with the PTM; $\rho_B/\rho_f=1/1000$. Also shown is the solution for the approximate capture time from Eq. (21).

vortex core, and are then forced by the vortex field to migrate towards the center of rotation as they are captured.

VI. NONCAVITATING BUBBLE CAPTURE PREDICTED WITH THE POINT-PARTICLE-TRACKING MODEL

The one-way coupled PTM was used to predict the time of capture for spherical bubbles by a Gaussian vortex, $t_C^*=t_C u_C/r_C$. An Euler integration scheme with time stepping was used to solve the horizontal and vertical components of Eq. (1). The case of noncavitating bubbles was first considered. Bubbles of varying sizes were released at different radial positions from the vortex axis r_X with an initial velocity equal to that of the fluid at the bubble center. A bubble was considered captured when it intersected the annulus defined by $1/4$ of the core radius, which approximately corresponded to the region of lowest core pressure. In these simulations, the bubble remained spherical (equivalent to $\mathrm{We}\ll 1$.)

For bubbles far away from the vortex, we can assume that the bubble accelerations and lift forces are negligible and that there exists a balance between the pressure gradient induced force and the drag force on the bubble, $V_B\nabla P \approx F_D$. If the largest component of the bubble velocity is in the radial direction $\mathbf{u}_{B,r}$, then the force balance far from the vortex axis becomes

$$\frac{-u_\theta^2(r)}{r}\rho_f\frac{4}{3}\pi R_O^3 \approx \frac{1}{2}\rho_f C_D \pi R_O^2 u_{B,r}^2, \tag{19}$$

where $u_\theta(r)\approx u_C r_C/\eta_2 r$ and $C_D\approx 12\nu_f/R_O u_{B,r}$. The bubble velocity becomes

$$u_{B,r}\approx -\frac{2(u_C r_C R_O)^2}{9\eta_2^2\nu_f}\frac{1}{r^3}. \tag{20}$$

This expression can be integrated to yield the approximate capture time for bubbles far from the vortex core, $r_X/r_C\gg 1$:

$$t_C^*\approx (u_C/r_C)\int_{r_X}^{0}\frac{1}{u_{B,r}(r)}dr=\frac{9\eta_2^2}{8\,\mathrm{Re}_C}\left(\frac{r_C}{R_O}\right)^2\left(\frac{r_X}{r_C}\right)^4. \tag{21}$$

The predicted capture times are shown in Fig. 2 for both Eq. (21) and the PTM. The approximation of Eq. (21) underpredicts the capture time in comparison to the PTM. In deriving Eq. (21) it is assumed that the bubble moves in a radial path. In reality, the bubble moves in a spiral path as it is captured. This results in increasing the effective radial component of the drag force in the PTM. The radial component of the drag force is underpredicted in the approximation, resulting in an underprediction of the capture time. However, the relationship reveals the trends in capture time with r_X/r_C, r_C/R_O, and Re_C. The pressure gradient induced force increases with R^3, while the drag force increases with R^2. Consequently, in regions of small bubble acceleration, smaller bubbles will take much longer to move toward the vortex center.

Once the bubble comes closer to the vortex axis, the lift and added mass forces become more important in the bubble motion. Figure 3 shows the capture time for the case with $\mathrm{Re}_C=u_C r_C/\nu=3\times 10^4$, which is equivalent to the experimentally measured vortex. The solution is shown for the four lift coefficients. The force on the bubble resulting from the local pressure gradient drives the bubble toward the vortex axis, while the drag, lift, and added mass forces act to retard the bubble motion.

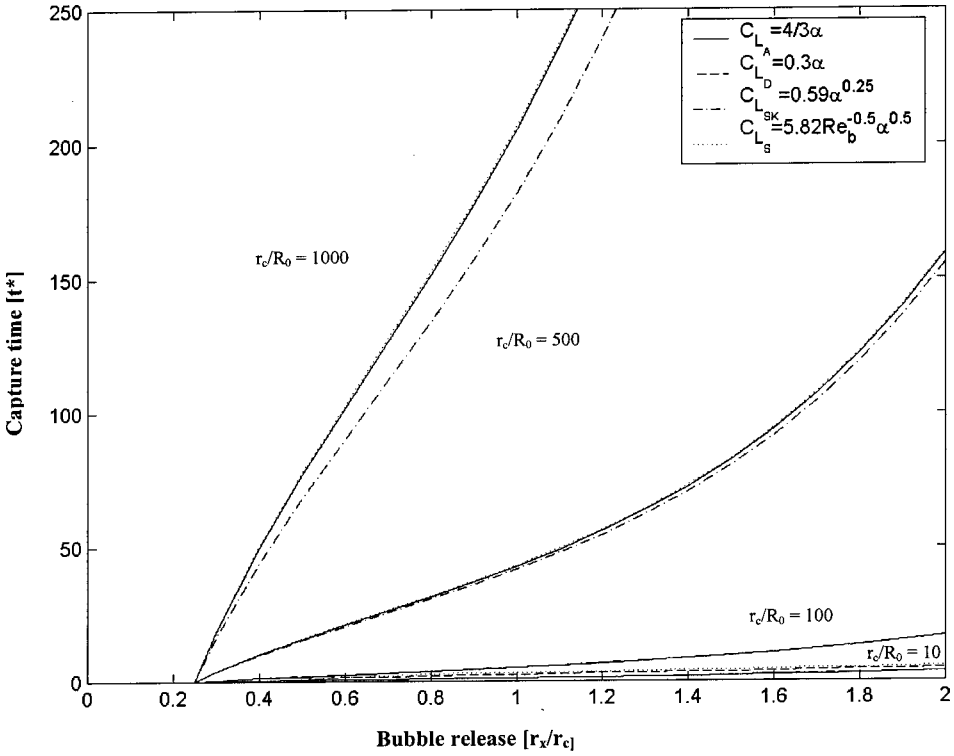

FIG. 3. Bubble capture time t^* vs the release position r_X/r_C using the four different lift coefficients C_l for varying bubble sizes r_C/R_O computed with the PTM; $\rho_B/\rho_f=1/1000$.

Variation in the lift coefficient leads to some change in the capture time, although the effect is secondary. We can scale the average bubble Reynolds number as

$$\mathrm{Re}_B \sim \frac{r_X}{t_C}\frac{R_O}{\nu_f} = \mathrm{Re}_C \frac{1}{t_C^*}\frac{R_O}{r_C}\frac{r_X}{r_C}. \tag{22}$$

Here, r_X/r_C is on the order of 1, t_C^* is on the order of 10, and Re_C is on the order of 10^4. Then the bubble Reynolds number Re_B will be on the order of $10(R_O/r_C)^{-1}$, and the bubble Reynolds number will decrease with increasing capture time and decreasing bubble size. The lift coefficients proposed by Saffman [Eq. (7)] is valid for $\mathrm{Re}_B<20$, and the largest bubbles approach this limit. The relationships proposed by Dandy and Dwyer [Eq. (8)] and Sridhar and Katz [Eq. (9)] are valid for somewhat higher bubble Reynolds numbers up to ≈ 100. The highest Re_B will occur in the last stages of capture.

The highest levels of vorticity occur for $r/r_C<2$, along with the highest bubbles slip velocities. The capture time when the bubble is within $r/r_C<2$ is on the order of unity, making the relative velocity on the order of u_C. The nondimensional shear in the core α_C can then be scaled as

$$\alpha_C = \frac{|\omega_C|R_O}{|\mathbf{u}-\mathbf{u}_B|} \sim \frac{2u_C R_O}{r_C}\frac{1}{u_C} = \frac{2R_O}{r_C}. \tag{23}$$

The highest local values of α_C occur within the vortex core, however. For the smallest bubbles considered here, $\alpha_C \ll 1$. For the largest bubbles considered here, α_C is between 0.1 and 1. The lift coefficients proposed by Auton [Eq. (6)] and Dandy and Dwyer [Eq. (8)] are for the case of $\alpha<1$, making them less appropriate for the final portion of the capture process of larger bubbles. Figure 4 shows the variation of the capture time with the vortex Reynolds number for the case of $r_C/R_O=50$, using the lift coefficient of Auton [Eq. (6)]. As expected, the time for bubble capture increases with increasing fluid viscosity and decreases approximately as $1/\mathrm{Re}_C$.

VII. DIRECT NUMERICAL SIMULATIONS OF NONCAVITATING BUBBLE CAPTURE

The PTM model does not account for bubble deformation and bubble-flow interaction that may occur during the final stages of collapse. It is expected that these effects are most important for relatively large bubbles as they near the vortex core. To examine this process, bubbles with r_C/R_O on the order of 10 were computed using DNS for various Weber and cavitation numbers. In these simulations, the effective vortex maximum tangential velocity and core size are $u_C=5$ m/s and $r_C=2.5$ mm, respectively. The length of the computational domain is four core radii, or 10 mm. The vortex Reynolds number $\mathrm{Re}_C=250$, is about 50 times lower than the experimentally examined vortex. However, even at the lower Reynolds number, the amount of vortex diffusion during the computation was relatively small, with the core growing less than 5% over the duration of the computation. The kinematic viscosity and density of the gas phase were 1/10 that of the fluid. This ratio was chosen to improve the computational efficiency. The initial bubble radius was made a proportion of the core radius, and the release position of the bubble was varied along the radius. Again, the bubble was given an initial velocity equal to the mean of the surrounding fluid. Bubbles were released at $y/L=0.5$ and varying x/L, with the vortex axis at $x/L=y/L=0.5$. A grid resolution study was performed for the capture of a noncavitating bubble with $r_C/R_O=8$ and $\mathrm{We}=0.13$. The bubble was released at $r_X/r_C=0.5$, a region of large flow gradients. Simulations with resolutions of 96^3, 128^3, 160^3 were compared,

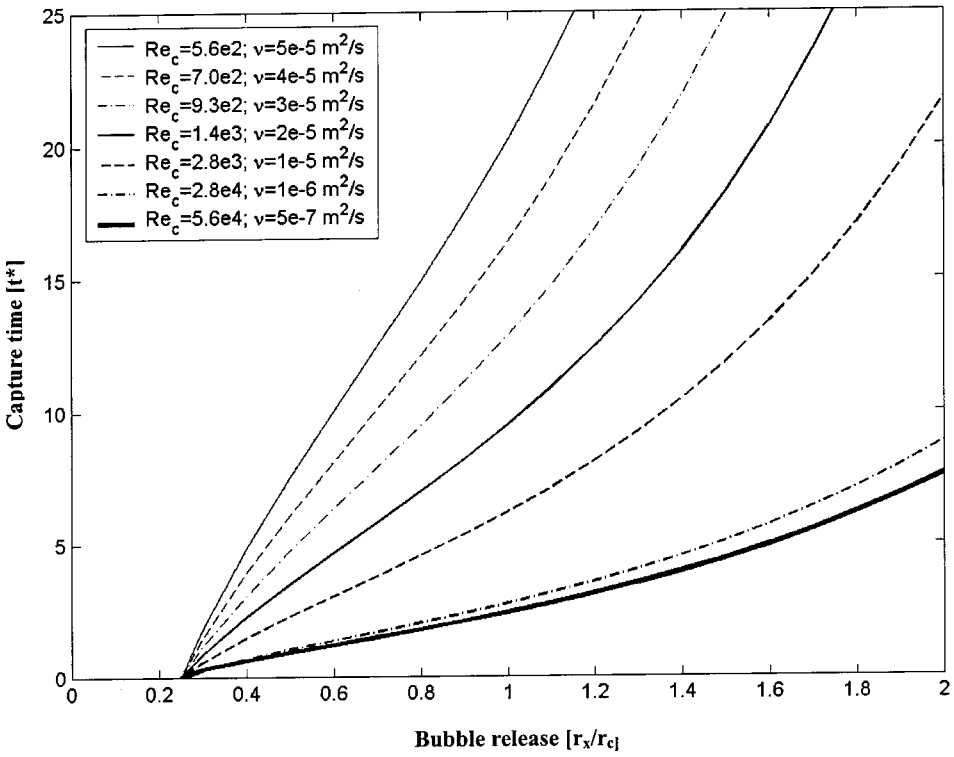

FIG. 4. Bubble capture time t^* vs the release position r_X/r_C for varying Reynolds number Re computed with the PTM; $\rho_B/\rho_f=1/1000$.

and bubble center positions at nondimensional time $t^*=1.77$ were within 1% of the domain length. It was concluded that a resolution of 128^3 would be sufficient. The time step was subject to restrictions due to the diffusion terms as well as the centered differencing used for the advection terms. These restrictions are $\Delta t\nu/\Delta x^2 \leqslant 1/8$; $[\Delta t(|U_x|+|U_y|+|U_z|)^2]/\nu \leqslant 8$. The minimum time step from the two relations was used in the simulations.

Figure 5(a) shows the trajectory of a noncavitating bubble with $r_C/R_O=8$ and We=0.13 for $r_X/r_C=1.0$, and Fig. 5(b) shows the vorticity in the *x*-*y* plane. It is clear that the bubble locally modifies the flow, and a wake develops behind the bubble. Figure 6 shows the trajectory of three bubbles released at $r_X/r_C=1.5$, 1.0, and 0.5 along with the prediction of the PTM. The Weber number in the DNS computations is 0.13, and $r_c/R_0=8$. Again, the bubble is considered captured when the bubble interface crosses $r_C/4$. The capture times predicted with the DNS for the three bubbles are $t^*=4.61$, 2.22, and 0.74. These are compared with $t^*=4.51$, 2.74, and 0.85 for the PTM. Here, the density ratio and vortex properties of the DNS calculation were used in the PTM, and the lift coefficient of Auton was used. The low Weber number in the DNS calculations leads to relatively little bubble deformation, and the capture times are within 20% of those from the PTM. This variation is on the order of the changes in the PTM prediction that result from the use of the different lift coefficients.

Table I presents a summary of the simulations and the capture times. The PTM both overpredicts and underpredicts the capture time compared to the DNS. The differences range between ±20% on average. When the bubbles start farther from the vortex, the PTM predicts a shorter capture time. But, when the bubbles start closest to the vortex, the PTM predicts a longer capture time. Moreover, these differences are more pronounced as the We increases. This suggests that the capture time is influenced by bubble deformations and bubble-flow interactions during the last stages of capture.

Figure 7 shows the trajectories and capture times for a bubble with $r_c/R_0=8$ for two different Weber numbers released at $r_X/r_C=1.5$. The capture time decreases with increasing Weber number, implying that increased bubble deformation leads to faster bubble capture. The capture times computed with the PTM and the DNS for $r_X/r_C=1.0$ (Table I) are similar. But the PTM underpredicts the capture times for bubbles released at $r_X/r_C=1.5$, suggesting the accumulated effect of varying lift coefficient on the final capture time. Figure 8 shows the capture of a bubble with $r_C/R_O=12$, We=0.1, and $r_X/r_C=1.5$. The trajectory of this bubble can be compared to the trajectory of the larger bubble ($r_C/R_O=8$) shown in Fig. 6 for similar We and r_X/r_C. The smaller bubble requires more turns to get captured, its trajectory better approaches the circular shape, and its capture time is longer than that for the large bubble (see also Table I). However, the PTM underpredicts the capture time for both bubble sizes, suggesting that the lift and drag coefficients of the PTM are too small when the bubble is close to capture, even though the lift coefficient used is the largest of the four considered.

VIII. THE CAPTURE OF CAVITATING NUCLEI

The capture of potentially cavitating nuclei is now considered. As the gas bubble experiences reduced pressure, its volume will increase isothermally. Bubbles far from the low-pressure region will grow quasistatically and isothermally ($k=1$) until $p(r) \leqslant p_V$, with the radius satisfying the equation

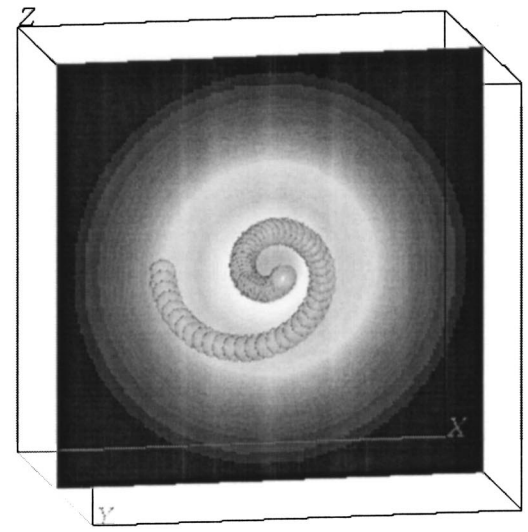

(a)

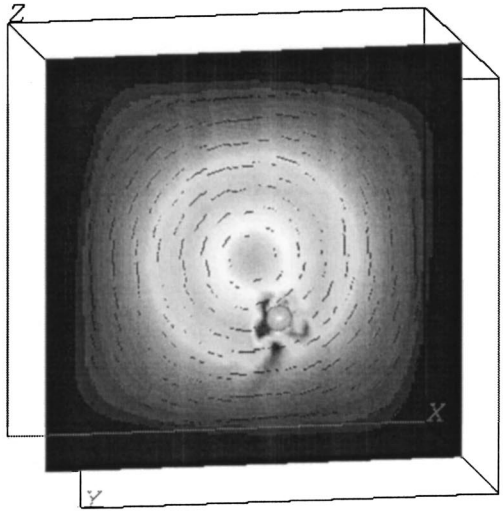

(b)

FIG. 5. (a) The DNS simulation of a noncavitating bubble being captured by a line vortex. $r_c/R_0=8$, We$=0.13$, and released at $r_x/r_c=1$. (b) The DNS simulation of the vorticity contours and the streamlines at $t^*=0.85$ with the same conditions as in (a), $\rho_B/\rho_f=1/10$.

$$p_V - p(r) + p_{GI}\left(\frac{R_O}{R(r)}\right)^3 - \frac{2\overline{\sigma}}{R_O}\frac{R_O}{R(r)} = 0. \tag{24}$$

As the pressure is decreased further, the bubble can begin to grow rapidly. A stability analysis of Eq. (10) yields the critical radius $R_i(r)$ above which bubbles will grow explosively for a given liquid tension (see Brennen[28] for a complete discussion):

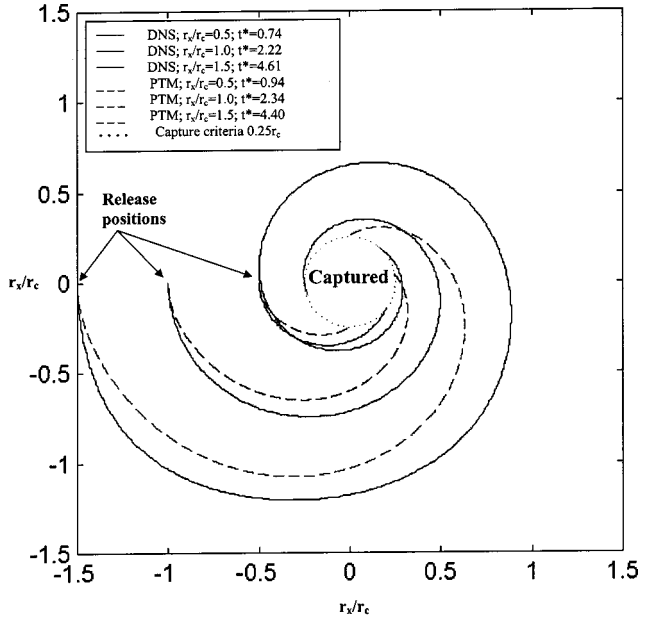

FIG. 6. The trajectory of a noncavitating bubble for three release positions, r_X/r_C, computed with the PTM and DNS (cases 1, 2, and 3 of Table I). $\rho_B/\rho_f=1/10$ for the PTM and DNS. The capture time criterion is $0.25r_C$.

$$R_i(r) \geqslant \frac{4\overline{\sigma}}{3[p_V - p(r)]}. \tag{25}$$

Vaporous cavitation can occur when the pressure at the vortex axis is less than or equal to the vapor pressure $p_C \leqslant p_V$. From the relationship for the core pressure [Eq. (15)] and our definition of σ_∞ [Eq. (18)], this is equivalent to the condition $\sigma_\infty \leqslant 2\eta_3/\eta_2^2 = \sigma_i = 3.40$, where σ_i is the cavitation inception index which is a property of the Gaussian vortex.

The static equilibrium radius can then be rewritten in terms of the cavitation and Weber numbers:

$$-\sigma_\infty + \left(\sigma_\infty + \frac{2}{\mathrm{We}}\right)\left(\frac{R_O}{R(r)}\right)^3 - \frac{2}{\mathrm{We}}\left(\frac{R_O}{R(r)}\right) + \frac{2f(r/r_C)}{\eta_2^2} = 0. \tag{26}$$

This expression is valid for $p(r) \geqslant p_V$ or equivalently,

$$-\sigma_\infty - \frac{2f(r/r_C)}{\eta_2^2} > 0. \tag{27}$$

The critical radius [Eq. (25)] can also be reformulated in terms of the Weber and the cavitation numbers:

$$\frac{R_i(r)}{R_O}\frac{\sigma_i \mathrm{We}}{4} = \left(\frac{1}{f(r/r_C)/\eta_3 - \sigma_\infty/\sigma_i}\right). \tag{28}$$

Small bubbles are expected to move toward the vortex axis, quasistatically changing volume until they reach a radial position r_i where $R_i(r_i)=R(r_i)$ when unstable bubble growth will occur.

Consequently, the parameters for nuclei capture are r_C, u_C, Re_C, r_X, R_O, We, and σ_∞. We will consider in the following theoretical analysis the bubble capture for the experimentally examined vortex, thus setting the first three parameters.

TABLE I. A summary of the computed bubble capture cases using PTM and DNS. The bubble to fluid density ratio and kinematic viscosity ratio are 1/10 for the DNS and PTM.

Case	Method	r_X/r_C	r_C/R_0	We	t^*	% of PTM
1	DNS	0.5	8	0.13	0.74	79
	PTM	0.5	8	···	0.94	
2	DNS	1.0	8	0.13	2.22	95
	PTM	1.0	8	···	2.34	
3	DNS	1.5	8	0.13	4.61	105
	PTM	1.5	8	···	4.40	
4a	DNS	1.5	8	0.1	4.86	110
4b	DNS	1.5	8	0.01	5.84	133
	PTM	1.5	8	···	4.40	
5	DNS	1.5	12	0.1	10.3	144
	PTM	1.5	12	···	7.13	
6a	DNS	1	8	1	1.91	82
6b	DNS	1	8	0.1	2.33	100
6c	DNS	1	8	0.01	2.51	107
	PTM	1	8	···	2.34	

The nuclei to be considered are $r_C/R_O=50$, 200, 500, and 1000 corresponding to bubbles of 110, 28, 11, and 6 μm radii. This corresponds to We=26, 6.5, 2.6, and 1.3 for air bubbles in clean water. We will consider free-stream cavitation numbers ranging from $\sigma_\infty/\sigma_i=1$, 7/8, 3/4, 1/2, to 1/4. It should be noted that, in practice, it is difficult to sustain large tensions in the vortex core for steady line vortices. When the tension is sufficiently high, even the smallest nu-

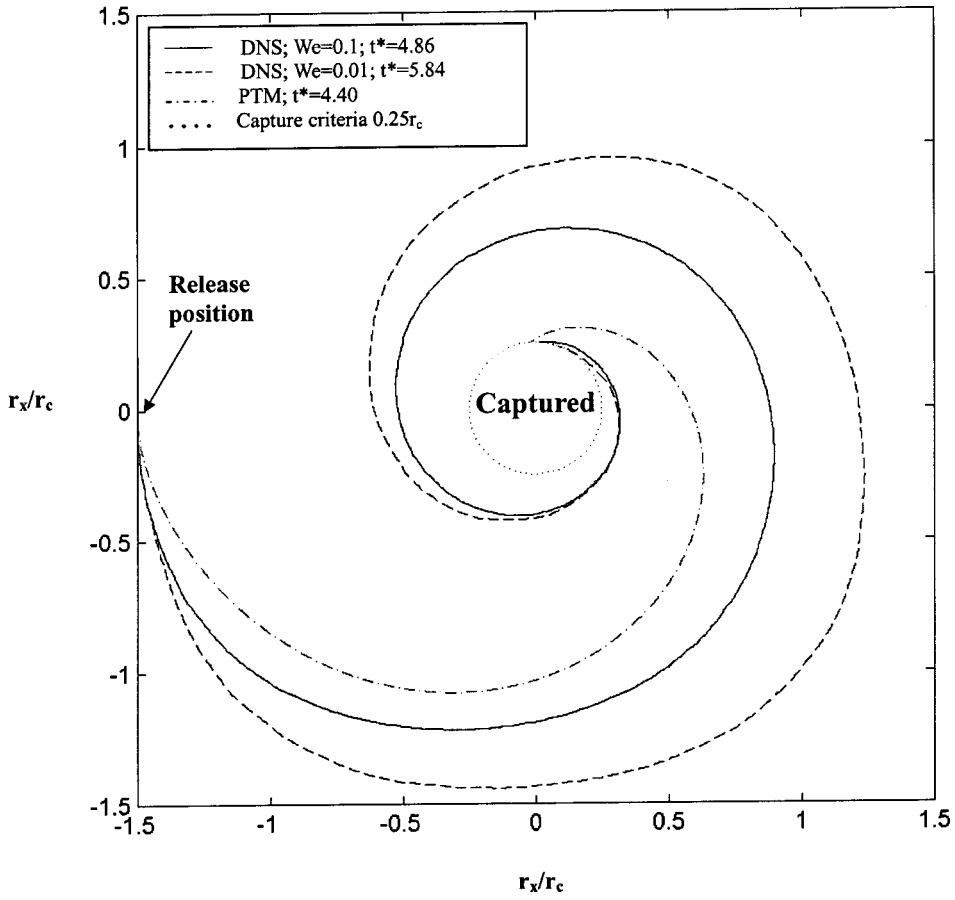

FIG. 7. The trajectory of a noncavitating bubble for varying Weber number We computed with the PTM and DNS. $\rho_B/\rho_f=1/10$ for the PTM and DNS [cases 4(a), and 4(b) of Table I]. The capture time criterion is $0.25r_C$.

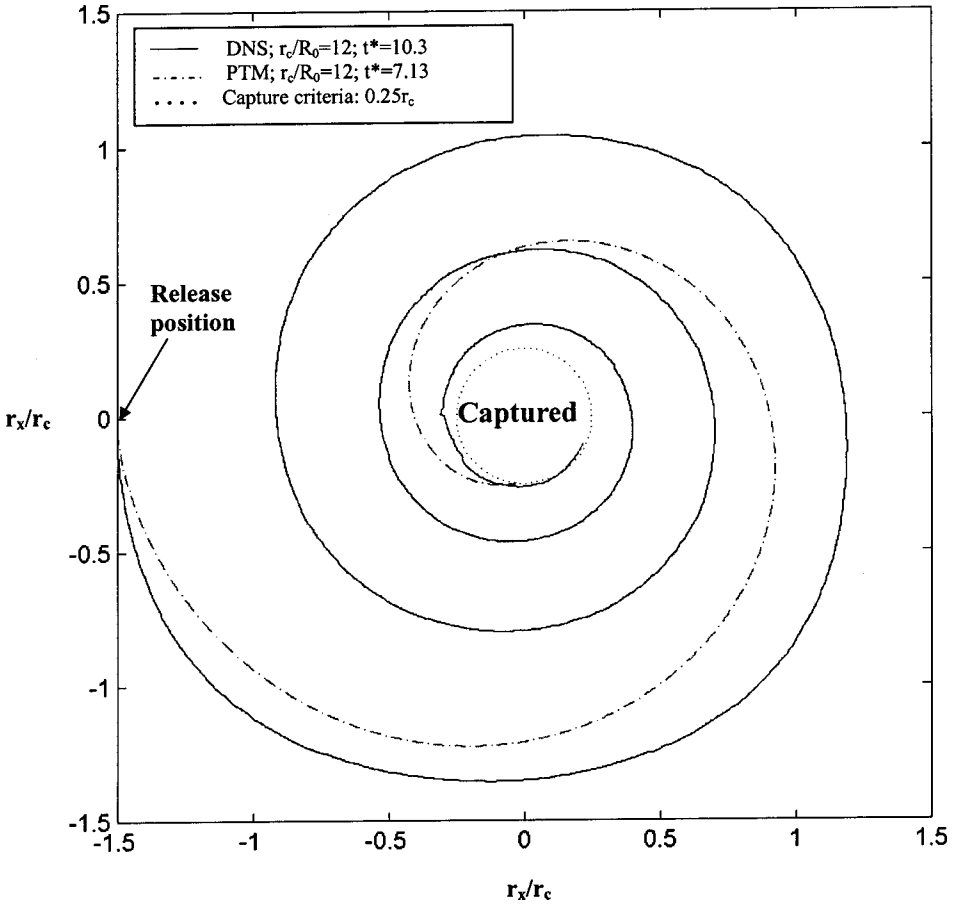

FIG. 8. The trajectory of a noncavitating bubble computed with the PTM and DNS. $\rho_B/\rho_f=1/10$ for the PTM and DNS (case 5 of Table I). The capture time criterion is $0.25r_C$.

clei will cavitate and the vortex core will fill with an annulus of vapor.

Solutions for $R_i(r/r_C)$ and $R(r/r_C)$ were computed for the four conditions described above. The vertical dashed line is the radial position when the fluid pressure reaches the vapor pressure. Figure 9 shows the case of $r_C/R_O=50$, the largest bubbles. As the bubbles come closer to the core, the equilibrium radius changes by a factor of up to 3 before inception. All of these bubbles are initially large enough to cavitate when they pass into the flow with pressure below

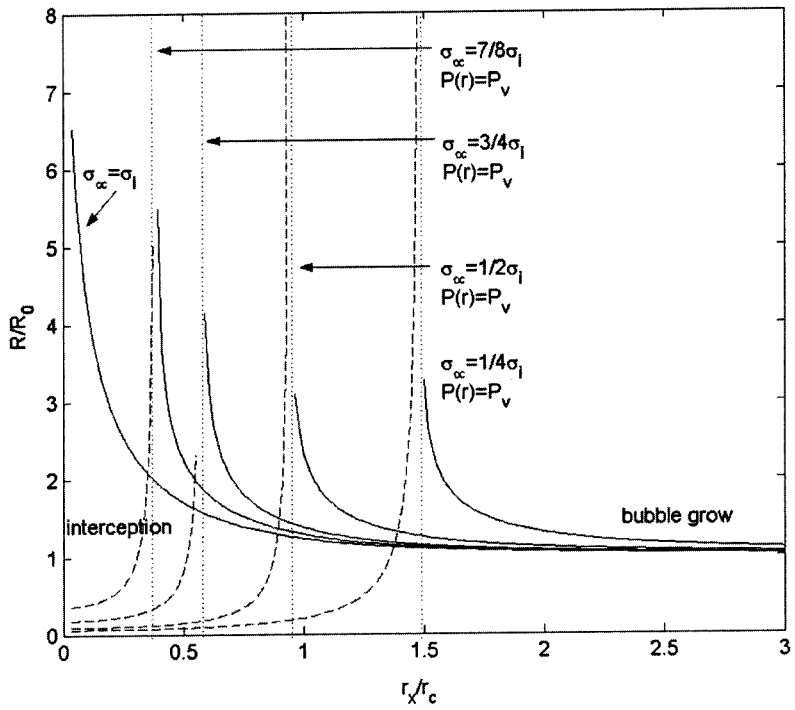

FIG. 9. The quasistatic growth of the bubble radius as a function of distance from the vortex axis for a bubble with an initial size $r_c/R_0=50$, We=26 for varying vortex cavitation numbers (solid lines). Also plotted is the solution of Eq. (29) (dashed lines), which yields the critical radius R_i for rapid bubble growth as a function of r_x/r_c for varying cavitation numbers. The vertical dotted lines occur when $p(r)=p_v$ for a given σ_∞. The pressure field is equivalent to that of the experimental vortex.

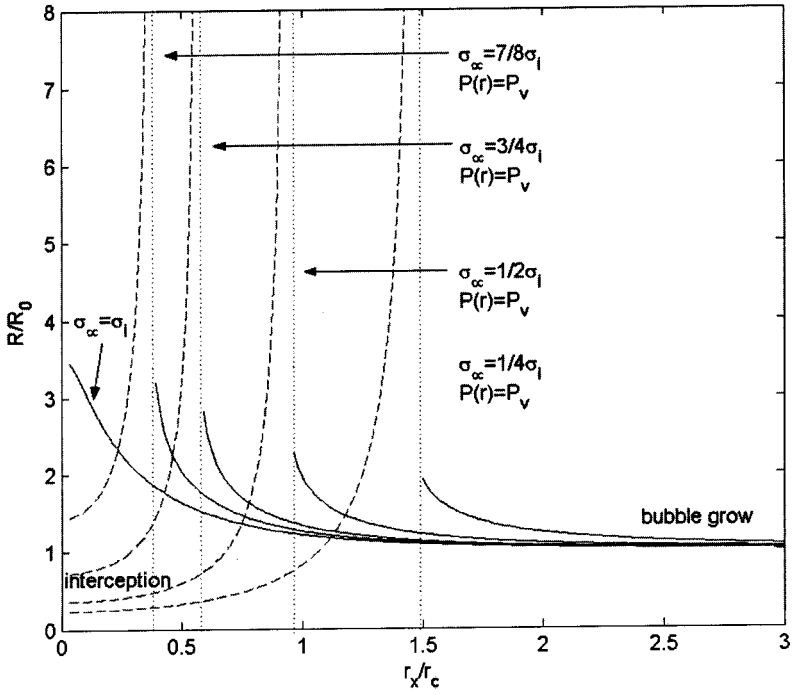

FIG. 10. Same as Fig. 9 but with $r_c/R_0=200$, We $=6.5$.

vapor pressure, even before the added volume increases as they approach the core. Figure 10 shows the case $r_C/R_O=200$. The quasistatic radius change of these bubbles is even smaller, about two times. But, even with this increase, the nuclei are still barely big enough to cavitate. Once they pass into the region of tension, they will continue to grow and will then cavitate after reaching the core for the lowest cavitation numbers. Finally, for the case of $r_C/R_O=1000$ in Fig. 11, the bubbles change their radii the least as they approach the core, and these small bubbles will only cavitate when the core pressure is in strong tension and after the bubbles have grown quasistatically.

The capture time of the cavitating nuclei will not differ significantly from that of the noncavitating case for bubbles that originate far from the vortex. Nonetheless, there exist some differences between the two cases. First, the capture criteria will differ, since the bubble can be considered captured once it begins to grow rapidly, and this can occur at a radius that is larger than $r_C/4$, the criteria chosen for the noncavitating capture. Second, as the bubbles begin to grow quasistatically, the rate of capture will increase. Third, as the bubbles begin to grow dynamically, the force due to volume changes [Eq. (4)] will retard the bubble's inward motion, but the relatively slow rate of the bubble volume change during

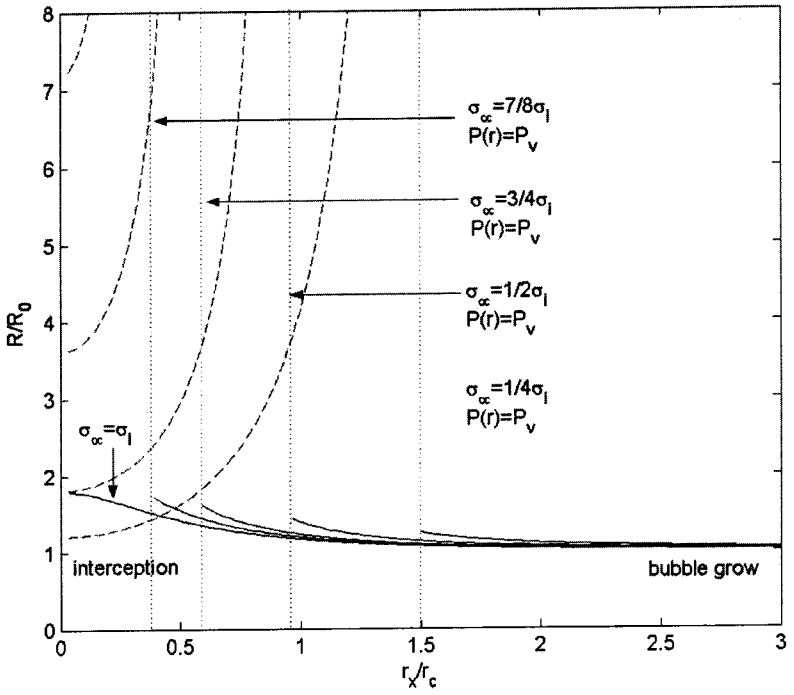

FIG. 11. Same as Fig. 9 but with $r_c/R_0=1000$, We $=1.3$.

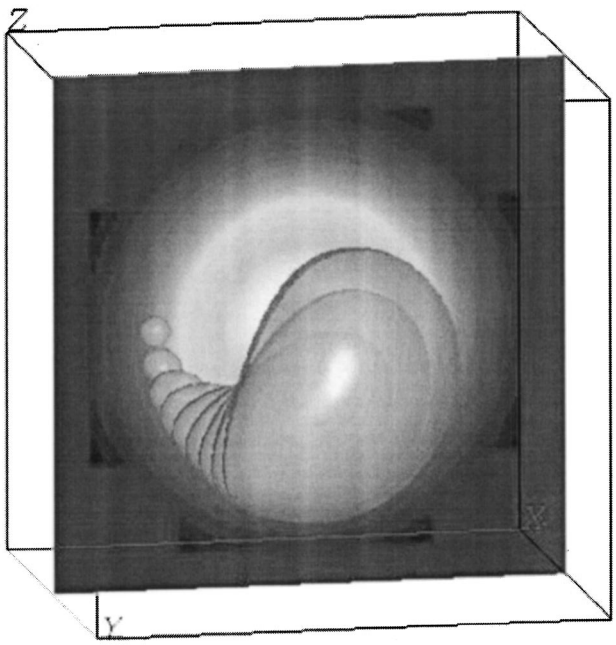

FIG. 12. The DNS simulation of a cavitating bubble being captured by a line vortex. $r_c/R_0=8$, We=24, $\sigma_\infty=1.0$, $\rho_B/\rho_f=1/10$. The bubble was initially in equilibrium and released at $r_x/r_c=1$.

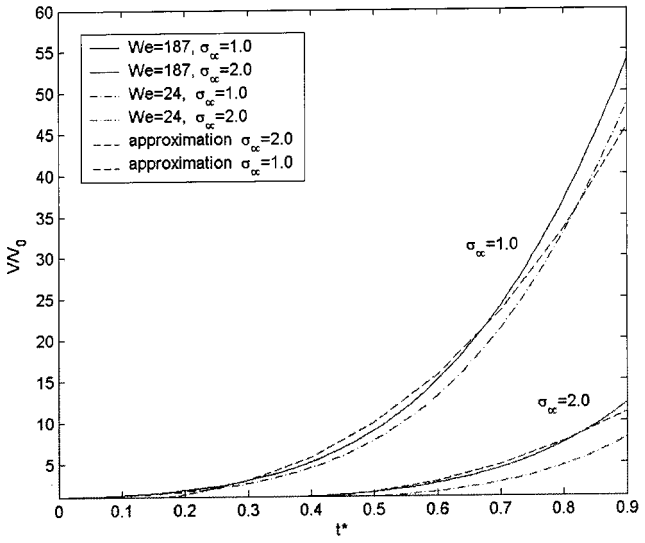

FIG. 13. The rate of volume growth for cavitating bubbles captured by a line vortex from the DNS simulation for varying We and σ_∞. $r_c/R_0=4$, and the bubble is initially in equilibrium and released at $r_x/r_c=1$. Also plotted is the offset asymptotic volume growth of a cavitating spherical bubble given by Eq. (31).

the quasistatic growth of the bubble makes this term negligible up until the rapid bubble growth. All of these effects are relatively small, but they lead to a decrease in the capture time Δt_C^* on the order of 1 for the larger bubbles. Otherwise, the capture time for the smaller bubbles is not substantially different between the cavitating and noncavitating cases, especially for bubbles starting far from the vortex core.

Figure 12 shows the DNS solution for cavitating bubble volume changes during the last part of the bubble capture. The simulation is for a bubble with an initial $r_C/R_O=8$, We=24, released at $r_X/r_C=0.6$. The cavitation number is $\sigma_\infty=1.0$ based on the pressure imposed at the computational boundary. Once the bubble begins to grow, it is pulled in toward the vortex axis and begins to deform. Figure 13 shows the volume history of the bubble for $\sigma_\infty=1.0$ and 2.0. Once a spherical bubble begins to grow rapidly, the asymptotic rate of radius growth is

$$\frac{dR}{dt} \approx \left(\frac{2}{3} \frac{(p_V - p_B)}{\rho_f} \right)^{1/2}. \tag{29}$$

Consequently, the volume should increase as

$$\frac{V(t)}{V_O} = \left[1 + \frac{t_G^*}{R_O} \frac{r_C}{u_C} \left(\frac{2}{3} \frac{(p_V - p_B)}{\rho_f} \right)^{1/2} \right]^3. \tag{30}$$

Also plotted in Fig. 13 is the volume growth predicted by Eq. (31), where $t^* = t_G^* - t_O^*$ with the offset $t_O^*=0.18$ and 0.45 for $\sigma_\infty=1.0$ and 2.0, respectively. These offsets are necessary to account for the time when the computed bubble begins to grow rapidly. Once the computed bubble begins to grow, the growth rate is approximately that of the asymptotic value, although the growth rate increases once the bubble is large and captured by the vortex.

IX. EXPERIMENTAL OBSERVATION OF BUBBLE CAPTURE AND GROWTH

The capture of bubbles was examined experimentally for the vortex described in Sec. V. The size of the bubble created varied with the laser power and the free-stream cavitation number. However, it was not possible to control the size of the bubble precisely. Figures 1(a) and 1(b) show eight images of a laser-induced bubble as it is captured by the vortex for $\sigma_C=3.0$. The vortex centerline and core radius are marked, and the time duration between the images is 350 μs. The experimental capture time as measured for multiple bubbles and the corresponding PTM predictions are shown in Fig. 14. The estimated uncertainty in the capture time is ±6%. The experimental vortex properties, and fluid densities ($\rho_B/\rho_f=1/1000$) and viscosities were used in this part of the PTM predictions.

The experimentally determined capture times fall within the PTM computed capture times given the variability of the initial bubble size, although the PTM model overpredicts the capture time somewhat. However, given the uncertainty in the bubbles diameter, and the possible influence of uncontrolled experimental parameters (e.g., the possible presence of axial flow in the vortex), the agreement between the experimental observations and the PTM predictions are encouraging. The bubbles under consideration can be considered cavitating nuclei, as their volume does grow as they enter the low-pressure region near the core. The process of bubble growth would slightly decrease the bubble capture time, as discussed above.

X. CONCLUSIONS

The capture of free-stream nuclei by a concentrated vortex has been studied using a PTM. DNS of bubble-vortex interaction were used to verify the accuracy of the PTM model. Moreover, experimental observations of the capture

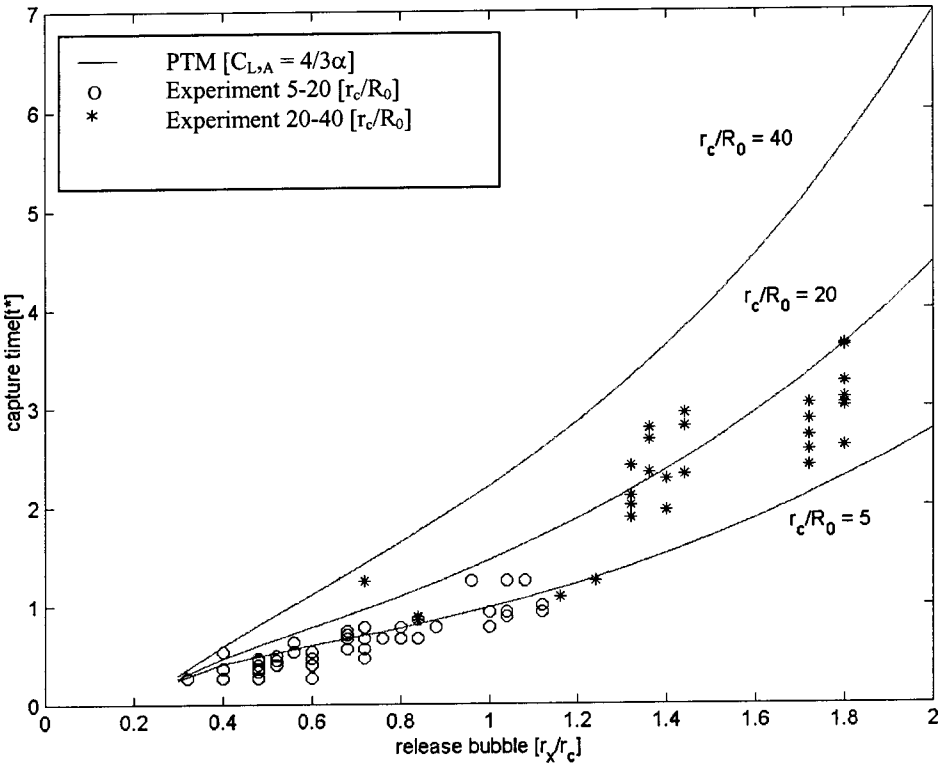

FIG. 14. Bubble capture time t^* vs the release position r_X/r_C for varying bubble sizes r_C/R_O computed with the PTM with $\rho_B/\rho_f = 1/1000$. Also shown is the experimental data for varying the release position r_X/r_C.

of laser induced bubbles by a concentrated vortex were used to assess the validity of the PTM model under like conditions. The conclusions of this study are as follows:

(1) The point-particle-tracking model can successfully predict the capture time for small bubbles starting far from a line vortex. The accuracy of the measured capture time decreases with decreasing release distance from the vortex axis. The DNS computations suggest that the PTM will underpredict the capture time in the final stages of capture when bubble deformations and bubble volume growth can become important.

(2) Varying the lift coefficient in the PTM produced little effect on the capture times.

(3) Smaller bubbles can orbit the vortex many times before being captured and thus take a longer time to migrate towards the vortex center. Their trajectories approach a circular shape.

(4) The capture time for a given bubble decreases with increasing the vortex-based Reynolds number.

(5) Bubble volume growth is very slow until the last stages of capture, which makes it useful to separate the process of cavitating nuclei capture into two steps; first the noncavitating capture of the nucleus and then the growth of the nucleus in the low-pressure core region. Thus, a noncavitating PTM model can be used to successfully predict the trajectory of cavitation nuclei up to the final staged of capture.

ACKNOWLEDGMENTS

This work was supported by the Office of Naval Research under Contract No. N00014-99-1-0307 with Dr. Ki-Han Kim, technical monitor. The DNS computations were conducted with the computational resources of the Maui High Performance Computing Center.

[1] R. E. A. Arndt, "Cavitation in vortical flows," Annu. Rev. Fluid Mech. **34**, 143 (2002).
[2] G. Sridhar and J. Katz, "Effect of entrained bubbles on the structure of vortex rings," J. Fluid Mech. **397**, 171 (1999).
[3] C. T. Hsiao and L. L. Pauley, "Study of tip vortex cavitation inception using Navier-Stokes computation and bubble dynamics model," J. Fluids Eng. **121**, 198 (1999).
[4] G. L. Chahine, "Non-spherical bubble dynamics in a line vortex," *Proceedings of the ASME FED Cavitation and Multiphase Flow Forum, Toronto*, edited by O. Furuya (Kluwer Academic, Dordrecht, 1990), Vol. 98, p. 121.
[5] G. L. Chahine, "Strong interactions bubble/bubble and bubble/flow," *Bubble Dynamics and Interface Phenomena*, edited by J. R. Blake, J. M. Boulton-Stone, and N. H. Thomas (Kluwer Academic, Dordrecht, 1994), p. 195.
[6] C. T. Hsiao and G. L. Chahine, "Numerical simulation of bubble dynamics in a vortex flow using Navier-Stokes computations and moving chimera grid scheme," Proceedings of 4th International Symposium on Cavitation, California Institute of Technology, Pasadena, CA, June 20–23, 2001.
[7] G. L. Chahine and C.-T. Hsiao, "Prediction of vortex cavitation inception using coupled spherical and non-spherical models," Proceedings of 24th Symposium of Naval Hydrodynamics, Fukuoka, Japan, July 8–13, 2002.
[8] M. R. Maxey and J. J. Riley, "Equation of motion for a small rigid sphere in a non-uniform flow," Phys. Fluids **26**, 883 (1983).
[9] J. Magnaudet and I. Eames, "The motion of high-Reynolds number bubbles in inhomogeneous flows," Annu. Rev. Fluid Mech. **32**, 659 (2000).
[10] N. Raju and E. Meiburg, "Dynamics of spherical particles in vortical and stagnation point flow fields," Phys. Fluids **9**, 299 (1997).
[11] W. L. Haberman and R. K. Morton, "An experimental investigation of the drag and shape of air bubbles rising in various liquids," DTMB Report No. 802, 1953.
[12] V. E. Johnson and T. Hsieh, "The influence of the trajectories of gas nuclei on cavitation inception," *Proceedings of the Sixth Symposium on Naval Hydrodynamics* (Office of Naval Research, Washington, DC, 1966), p. 163.
[13] T. R. Auton, "The lift on a spherical body in a rotational flow," J. Fluid

Mech. **183**, 199 (1987).
[14]T. R. Auton, J. C. R. Hunt, and M. Prud'homme, "The force exerted on a body moving in an inviscid unsteady non-uniform rotational flow," J. Fluid Mech. **183**, 241 (1988).
[15]P. G. Saffman, "The lift on a small sphere in a slow shear flow," J. Fluid Mech. **22**, 385 (1965).
[16]D. S. Dandy and H. A. Dwyer, "A sphere in shear flow at finite Reynolds number: Effect of shear on particle lift, drag, and heat transfer," J. Fluid Mech. **216**, 381 (1990).
[17]G. Sridhar and J. Katz, "Lift and drag forces on microscopic bubbles entrained by a vortex," Phys. Fluids **7**, 389 (1995).
[18]G. F. Oweis, J. Choi, and S. L. Ceccio, "Dynamics and noise emission of laser induced cavitation bubbles in a vortical flow field," J. Acoust. Soc. Am. **115**, 1049 (2004).
[19]A. Kubota, H. Kato, and H. Yamaguchi, "A new modeling of cavitating flows; a numerical study of unsteady cavitation on a hydrofoil section," J. Fluid Mech. **240**, 59 (1992).
[20]M. Deshpande, J. Feng, and C. Merkle, "Numerical modeling of thermodynamic effects of cavitation," ASME J. Fluids Eng. **119**, 420 (1997).
[21]S. O. Unverdi and G. Tryggvason, "A front-tracking method for viscous, incompressible, multi-fluid flows," J. Comput. Phys. **100**, 23 (1992).
[22]A. Esmaeeli and G. Tryggvason, "Direct numerical simulations of bubbly flows. Part 1. Low Reynolds number arrays," J. Fluid Mech. **377**, 313 (1998).
[23]A. Esmaeeli and G. Tryggvason, "Direct numerical simulations of bubbly flows. Part 2. Moderate Reynolds number arrays," J. Fluid Mech. **385**, 325 (1999).
[24]P. W. Yu, S. L. Ceccio, and G. Tryggvason, "The collapse of a cavitation bubble in shear flows—A numerical study," Phys. Fluids **7**, 2608 (1995).
[25]G. Trggvason, B. Bunner, A. Esmaeeli, D. Juric, N. Al-Rawahi, W. Tauber, J. Han, S. Nas, and Y.-J. Jan, "A front tracking method for the computations of multiphase flow," J. Comput. Phys. **169**, 708 (2001).
[26]O. Boulon, M. Callenaere, J.-P. Franc, and J.-M. Michel, "An experimental insight into the effect of confinement on tip vortex cavitation of an elliptical hydrofoil," J. Fluid Mech. **390**, 1 (1999).
[27]G. F. Oweis and S. L. Ceccio, "Instantaneous and time averaged flow fields of multiple vortices in the tip region of a ducted propulsor," Exp. Fluids (to be published).
[28]C. E. Brennen, *Cavitation and Bubble Dynamics* (Oxford University Press, New York, 1995).